SIAM J. APPL. MATH.
Vol. 83, No. 3, pp. 1146–1171

THE DYNAMICS OF A COLLAPSING POLYELECTROLYTE GEL*

GIULIA L. CELORA†‡, MATTHEW G. HENNESSY‡§, ANDREAS MUENCH‡, BARBARA WAGNER¶, AND SARAH WATERS‡

Abstract. We analyse the dynamics of different routes to collapse of a constrained polyelectrolyte gel in contact with an ionic bath. The evolution of the gel is described by a model that incorporates non-linear elasticity, Stefan–Maxwell diffusion and interfacial gradient free energy to account for phase separation of the gel. A bifurcation analysis of the homogeneous equilibrium states reveals three solution branches at low ion concentrations in the bath, giving way to only one above a critical ion concentration. We present numerical solutions that capture both the spatial heterogeneity and the multiple timescales involved in the process of collapse. These solutions are complemented by two analytical studies. Firstly, a phase-plane analysis that reveals the existence of a depletion front for the transition from the highly swollen to the new collapsed equilibrium state. This depletion front is initiated after the fast ionic diffusion has set the initial condition for this time regime. Secondly, we perform a linear stability analysis about the homogeneous states that show that for a range of ion concentrations in the bath, spinodal decomposition of the swollen state gives rise to localized solvent-rich(poor) and, due to the electroneutrality condition, ion-poor(rich) phases that coarsen on the route to collapse. This dynamics of a collapsing polyelectrolyte gel has not been described before.

Key words. polyelectrolyte gel, collapse, phase-space analysis, spinodal decomposition, stability analysis

MSC codes. 74N20, 74F10, 35B35

DOI. 10.1137/21M1419726

1. Introduction.

Ever since the seminal papers by Tanaka [38] and Dusek and Patterson [12], research on swelling and collapse of polyelectrolyte gels has been very intensive, both theoretically and experimentally [8, 7, 18, 27, 29]. These systems, combining elements of electrochemistry and condensed matter physics, display intriguing and subtle properties motivating both experimental and theoretical studies to understand their rich behavior. These gels also have a wealth of technological applications, and a better understanding of polyelectrolyte gels serves as a basis for developing smart, responsive materials and sensors [2, 5, 16, 37], for example. In particular, research in this field is driven by applications in medicine [16, 23], e.g., for drug delivery and tissue engineering. Additionally, polyelectrolyte gels are used as a model system for many types of biological tissues [25, 30] or in the modelling of mucus [24, 36] to gain fundamental insight into diverse phenomena in biology. Polyelectrolytes also serve as a model for bio-macromolecules, such as DNA and RNA [13, 32, 41].

*Received by the editors June 8, 2021; accepted for publication (in revised form) November 14, 2022; published electronically June 7, 2023.
https://doi.org/10.1137/21M1419726
Funding: The second author recognizes support from the Mathematical Institute through a Hooke fellowship, and the first author acknowledges the EPSRC and MRC Centre for Doctoral Training in Systems Approaches to Biomedical Science and Cancer Research UK for funding.

†Department of Mathematics, University College London, Gordon Street, London, WC1H 0AY, UK (g.celora@ucl.ac.uk).
‡Mathematical Institute, University of Oxford, Oxford OX2 6GG, UK (hennessy@maths.ox.ac.uk, muench@maths.ox.ac.uk, waters@maths.ox.ac.uk).
§Department of Engineering Mathematics, University of Bristol, Bristol BS8 1TW, UK (matthew.hennessy@bristol.ac.uk).
¶Weierstrass Institute, 10117 Berlin, Germany (wagnerb@wias-berlin.de).

In its simplest form, a polyelectrolyte gel is a network of covalently cross-linked polyelectrolyte macromolecules, that is, of polymer chains carrying fixed charges of the same sign, immersed in a solvent. If placed in an ionic bath, the gel will approach a new equilibrium state driven by osmotic effects and will swell or shrink [18]. This process depends on factors such as the concentration and valency of the salt in the solvent, the (nonlinear) elasticity of the gel, the concentration of fixed charges and the number of ionizable groups of the polyelectrolyte macromolecule, as well external fields, such an applied electric field or the temperature [22]. The change in volume does not always proceed continuously [1, 29, 40]. The discontinuous volume phase transition typically considers a gel that is divided into coexisting subdomains that are in thermodynamic equilibrium with jump conditions imposed at their interfaces [9, 3].

Unlike nonionic hydrogels [15, 33, 39], subtle changes in the environment surrounding the gel, such as increasing the ion concetration, can have a dramatic effect and result in discontinuous phase transitions connected with supercollapse [21, 19] and reentrant swelling [35]. A deeper understanding of these phenomena, in particular when comparing to experiments, is obtained with a model that resolves the pattern forming instabilities of the gel and the transient dynamics between equilibrium states over a large range of temporal and spatial scales. This will then shed light on the pattern formation processes leading to collapse [26, 42].

The governing equations of such a model are given in a companion paper [4], where we use nonequilibrium thermodynamics to systematically derive a phase-field model of a polyelectrolyte gel. That model accounts for the free energy of the internal interfaces which form on phase separation, as well as for finite elasticity, together with multicomponent transport models via Stefan–Maxwell diffusion. We also derive a thermodynamically consistent model for the ionic bath surrounding the gel. The electroneutral limit of the full three-dimensional model has been derived via matched asymptotic expansions [14] from which we obtain the jump conditions that need to be imposed at the gel-bath interface. First results from numerical simulations for a one-dimensional constrained gel have been presented in [4], where the possibility of spinodal decomposition—that is, a parameter regime where the uniform equilibrium solution is linearly unstable and hence phase separates in response to infinitesimal perturbations—is raised for the case of a *swelling* gel. Chen, Calderer, and Mori [6] and Mori et al. [28] also derived and analyzed a coupled model for a polyelectrolyte gel in contact with an ionic bath but do not consider phase separation.

The main goal of this study is to investigate the evolution of collapse via a volume phase transition in a constrained gel by a combination of mathematical techniques. First, we consider the nonlinear equations that determine the homogeneous equilibrium states and deduce the bifurcation that leads to the collapse as the salt concentration in the bath is raised. The numerical solution then reveals the fast initial transients that change the charge distribution in the gel, followed by the appearance of a (solvent) depletion front. This in turn we study via a phase-plane analysis. We systematically investigate the stability of the homogeneous states. This reveals a second route to collapse, where the gel first undergoes spinodal decomposition before the depletion front moves through the heterogeneous state.

The paper is structured as follows. In section 2, we introduce the electroneutral version of the model for a polyelectrolyte gel, previously derived in [4]. In section 3, we specialize the model to the case of a one-dimensional constrained gel in contact with an ionic bath, where the thin electric double layer between gel and bath is replaced by corresponding boundary conditions [14]. In section 4, we determine the bifurcation diagram for the homogeneous equilibrium states which are controlled by

the salt concentration in the bath and give an overview of various routes to collapse. We carry out numerical simulations that demonstrate the fast dynamics of the free ions that sets the stage for collapse via a moving depletion front. In section 5, we show the existence of this moving front via a phase-plane analysis. Section 6 investigates different parameter regimes that show spinodal decomposition. We use linear stability analysis that identifies parameter regimes for spinodal decomposition into localized solvent-rich(poor) phases that eventually coarsen on their path to collapse. In section 7, we draw our conclusions and give an outlook on further research directions.

2. Governing equations for a polyelectrolyte gel. We consider the problem of a polyelectrolyte gel swelling in a solution (the bath) containing a binary salt. The governing equations are systematically derived in [4], which extends previous models by Drozdov et al. [11] and Hong, Zhao, and Suo [17]. In particular, we include the gradient energy to account for the dynamics of collapse and phase separation. As standard in the literature, we consider the electroneutral formulation of the model. In Hennessy et al. [14], we give a detailed derivation of this limit via singular perturbation analysis, where we assume that the Debye length and thus the thickness of the double layer at the free interface between the gel and the bath is small compared to the size of the gel.

The governing equation are presented for the full three-dimensional problem in terms of the Eulerian coordinates associated with the current (deformed) configuration. The gel is described as a mixture of three phases: solvent (s), free ions ($+$ and $-$), and the charged polymer network (n). We assume that the fixed charges (with valence z_f) on the polymer network are evenly distributed on the network and account for a fixed fraction $\alpha_f < 1$ of the network volume. In this work, we consider z_f to be positive so that the positive ionic species in the solution (with valence z_+) will be denoted as co-ions ($+$), while the negative ones (with valence z_-) will be the counter-ions ($-$). As standard in the polyelectrolyte gel literature, we will assume in what follows that all mobile species (i.e., the solvent and ions) have the same molecular volume ν.

Let us denote by t time and $\boldsymbol{x} = (x, y, z)$ the Eulerian coordinates, while $\boldsymbol{X} = \boldsymbol{X}(\boldsymbol{x}, t)$ are the corresponding Lagrangian coordinates. Then the gel kinematics are described by the deformation gradient tensor $\mathbf{F} = (\partial \boldsymbol{X}/\partial \boldsymbol{x})^{-1}$, with its determinant $J = \det \mathbf{F}$ representing the volume expansion of the gel compared to the dry reference state, where $J = 1$. The velocity of the polymer network $\boldsymbol{v}_n$ can be expressed as

$$\boldsymbol{v}_n = -\mathbf{F}\frac{\partial \boldsymbol{X}}{\partial t}. \tag{2.1}$$

The composition of the gel is described in terms of volume fractions $\phi_i = \phi_i(\boldsymbol{x}, t)$ with $i \in \{s, +, -, n\}$. Assuming there are no voids in the gel, the volume fractions satisfy

$$1 = \phi_n + \phi_s + \phi_+ + \phi_-. \tag{2.2a}$$

Moreover, all of the phases are assumed to be incompressible; consequently, J is related to the network volume fraction ϕ_n by $J = \phi_n^{-1}$. The volume fraction occupied by fixed charges is $\phi_f = \alpha_f \phi_n$, where α_f indicates, as defined above, the fraction of volume of the network phase occupied by fixed charges. Since we assume the gel is electrically neutral at each location in space, its net charge must be zero. This introduces the additional constraint

$$z_f \phi_f + z_+ \phi_+ + z_- \phi_- = 0. \tag{2.2b}$$

Conservation of mass and momentum are given by

$$\partial_t \phi_n + \nabla \cdot (\phi_n \boldsymbol{v}_n) = 0, \tag{2.2c}$$

$$\partial_t \phi_m + \nabla \cdot (\phi_m \boldsymbol{v}_n) = -\nabla \cdot \boldsymbol{j}_m, \tag{2.2d}$$

$$\nabla \cdot \mathbf{T} = 0 \tag{2.2e}$$

for $m \in \mathbb{M} = \{s, +, -\}$. Here, $\mathbf{T}$ denotes the Cauchy stress tensor (to be specified below), and $\boldsymbol{j}_m$ are the volumetric fluxes of mobile species relative to the network that moves with velocity $\boldsymbol{v}_n$. By differentiating (2.2a) and (2.2b) with respect to time and using (2.2c)–(2.2d), we obtain

$$\nabla \cdot \left(\boldsymbol{v}_n + \sum_{m \in \mathbb{M}} \boldsymbol{j}_m \right) = 0, \tag{2.2f}$$

$$\nabla \cdot \left(z_+ \boldsymbol{j}_+ + z_- \boldsymbol{j}_- \right) = 0, \tag{2.2g}$$

which are used to replace (2.2c) and (2.2d) for the counter-ion fraction ϕ_-.

To complete the model, constitutive relations are required. The fluxes are described via Stefan–Maxwell diffusion to account for the relative friction between ions and solvent,

$$\boldsymbol{j}_s = -\phi_s K \left(\nabla \mu_s + \frac{\phi_+}{\phi_s} \nabla \mu_+ + \frac{\phi_-}{\phi_s} \nabla \mu_- \right), \tag{2.3a}$$

$$\boldsymbol{j}_\pm = -\frac{\mathcal{D}_\pm \phi_\pm}{k_B T} \nabla \mu_\pm + \frac{\phi_\pm}{\phi_s} \boldsymbol{j}_s, \tag{2.3b}$$

where μ_s, μ_+, and μ_- denote the (electro)chemical potentials of the mobile species, T is the temperature, k_B is the Boltzmann constant, $K = \mathcal{D}_s/(k_B T)$ is the solvent permeability, and $\mathcal{D}_m$ are the diffusivities of the mobile ions, where we consider $\mathcal{D}_+ = \mathcal{D}_- = \mathcal{D} > \mathcal{D}_s$ in line with the characteristic values reported (see supplementary material (suppmats.pdf [local/web 295KB]) Table SM1 and the literature cited therein [34, 11]). Furthermore, we have the following expressions for the three chemical potentials:

$$\mu_s = \mu_s^0 + \nu p - \frac{\gamma}{\nu} \nabla^2 \phi_s + k_B T \left[\ln(\phi_s) + \frac{\chi(1 - \phi_s)}{J} + \frac{1}{J} \right], \tag{2.3c}$$

$$\mu_\pm = \mu_\pm^0 + \nu p + z_\pm e \Phi + k_B T \left[\ln(\phi_\pm) - \frac{\chi \phi_s}{J} + \frac{1}{J} \right], \tag{2.3d}$$

where μ_m^0 are reference chemical potentials, Φ is the electric potential, p is the pressure, e is the elementary charge, χ is the temperature-dependent Flory interaction parameter, and γ is the interfacial stiffness parameter. The latter is associated with the free energy cost of internal interfaces separating regions of low and high solvent concentration. The pressure dependence of the ionic chemical potentials (2.3d) is a result of accounting for the ionic volume fractions in the no-void condition (2.2a) when deriving the model using an energy-imbalance inequality; see Celora et al. [4] for details. The pressure dependence of all of the chemical potentials allows stress-assisted diffusion to be captured in the model. For the stresses in the gel, we consider three contributions:

$$\mathbf{T} = -p\mathbf{I} + \mathbf{T}_K + \mathbf{T}_E. \tag{2.3e}$$

The first represents an isotropic stress from the fluid pressure with $\mathbf{I}$ denoting the identity tensor, while $\mathbf{T}_K$ represents the Korteweg stress generated at internal interfaces (i.e., gradients of the solvent concentration),

$$\mathbf{T}_K = \frac{\gamma}{\nu^2}\left[\left(\frac{|\nabla\phi_s|^2}{2} + \phi_s\nabla^2\phi_s\right)\mathbf{I} - \nabla\phi_s \otimes \nabla\phi_s\right], \tag{2.3f}$$

and $\mathbf{T}_E$ is the elastic stress from the response of a neo-Hookean polymer network

$$\mathbf{T}_E = \frac{G\,(\mathbf{B}-\mathbf{I})}{J}, \tag{2.3g}$$

where $\mathbf{B} = \mathbf{F}\mathbf{F}^T$ is the left Cauchy–Green tensor and G is the shear modulus. To close the system, we further need boundary and initial conditions which we derive next for the problem of a constrained gel, which is the focus of this study.

3. Specialization to constrained swelling and collapse. We consider the case of a constrained gel with monovalent fixed charges ($z_f = +1$) which undergoes uniaxial deformation (in the z direction) due to the uptake or release of a monovalent ($z_\pm = \pm 1$) salt solution (see Figure 1). This is analogous to the scenario considered in [9, 15] for the study of constrained swelling and deswelling of neutral hydrogels.

The gel is assumed to be attached to a substrate at $z = 0$, while the interface at $z = h(t)$ is free to move along frictionless side walls that do not influence the bulk behavior (see [15] for more details). The problem can be reduced to a one-dimensional Cartesian geometry, where the deformation gradient tensor $\mathbf{F}$ and the stress tensor $\mathbf{T}$ have the form

$$\mathbf{F} = \mathrm{diag}(1, 1, J(z,t)), \quad \mathbf{T} = \mathrm{diag}(T_\ell(z,t), T_\ell(z,t), T_{zz}(z,t)) \tag{3.1}$$

and the diffusive fluxes and network velocity are given by $\boldsymbol{j}_m = j_m(z,t)\boldsymbol{e}_z$ and $\boldsymbol{v}_n = v_n(z,t)\boldsymbol{e}_z$ respectively, with $\boldsymbol{e}_z$ representing the unit vector in the z direction. Moreover, all variables in (2.2)–(2.3) are assumed to only depend on z and t. At $z = 0$, we assume that the gel is bounded by a solid, insulated, impermeable substrate; hence,

$$v_n(0,t) = 0, \quad j_s(0,t) = 0, \quad j_\pm(0,t) = 0. \tag{3.2a}$$

Given the fourth-order derivative in the solvent fraction that ultimately arises from the interfacial term in the solvent chemical potential (2.3c), we need an additional condition on ϕ_s. We assume the solvent is neutral to substrate, resulting in [31]

$$\partial_z\phi_s(0,t) = 0. \tag{3.2b}$$

In most scenarios considered in this paper, we assume that the free surface of the gel at $z = h(t)$ is in contact with an ionic and electroneutral bath, which behaves like

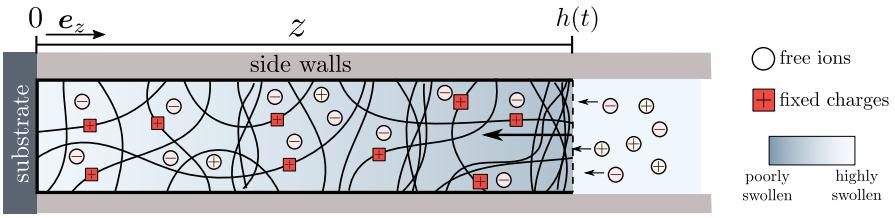

FIG. 1. *Schematic of a laterally confined polyelectrolyte gel that collapse along the z-axis only. The free interface with the bath is located at $z = h(t)$. As solvent is expelled by the gel, the free interface moves toward the left, and salt ions are absorbed/desorbed by the gel so as to maintain electroneutrality of the gel.*

an infinite reservoir of ions. For this scenario, we adapt the boundary conditions derived in [14] starting from the full nonelectroneutral model via singular perturbation analysis to account for the formation of a small layer, known as the electric double layer, near the free interface where electroneutrality breaks down. Away from the interface with the gel, the volume fraction of ions in the bath is controlled experimentally and set to the value ϕ_0. In our one-dimensional situation and assuming the electric potential is zero in the bath, we have

$$T_{zz}(h(t),t) = 0, \tag{3.3a}$$

$$\partial_z \phi_s(h(t),t) = 0, \tag{3.3b}$$

$$\mu_{\pm}(h(t),t) = \mu_{\pm}^0 + k_B T \ln(\phi_0), \tag{3.3c}$$

$$\mu_s(h(t),t) = \mu_s^0 + k_B T \ln(1-2\phi_0). \tag{3.3d}$$

To close the system, we further specify a kinematic condition for the boundary $z = h(t)$, which here moves with the gel velocity such that

$$\frac{dh}{dt} = v_n(h(t),t). \tag{3.3e}$$

Having specified the geometry and boundary conditions for the problem, we nondimensionalize the system as follows:

$$\begin{gathered} \hat{\mu}_m = \frac{\mu_m - \mu_m^0}{k_B T}, \quad \hat{\Phi} = \frac{\Phi e}{k_B T}, \quad \hat{\mathbf{T}} = \frac{\mathbf{T}}{G}, \qquad \hat{z} = \frac{z}{L}, \\ \hat{t} = \frac{t}{\tau}, \quad \hat{p} = \frac{p}{G}, \qquad \hat{j}_m = \frac{\nu L}{\mathcal{D}_s} j_m, \qquad \tau = \frac{L^2}{\mathcal{D}_s}, \end{gathered} \tag{3.4}$$

where $m \in \mathbb{M}$ and L is the characteristic size of the gel. The system possesses a second natural length scale, $L_{\text{int}} = \sqrt{\gamma/(\nu k_B T)}$, which characterizes the thickness of the internal interfaces that can occur via phase separation of the gel into highly and poorly swollen regions. The ratio of these two length scales gives rise to the nondimensional parameter $\omega = L_{\text{int}}/L$. Further nondimensional material parameters are

$$\mathcal{G} = \frac{\nu G}{k_B T}, \quad \hat{\mathcal{D}} = \frac{\mathcal{D}}{\mathcal{D}_s}. \tag{3.5}$$

Note that $\mathcal{G}$ can be related to the number density of polymer chains N_p in the dried network via $\mathcal{G} = N_p \nu$, which helps in the estimation of its value (see Table SM1). We introduce the scalings into the one-dimensional model and then drop the hat notation so that the nondimensional governing equations read

$$\partial_t \phi_s + \partial_z(\phi_s v_n) = -\partial_z j_s, \tag{3.6a}$$

$$\partial_t \phi_+ + \partial_z(\phi_+ v_n) = -\partial_z j_+, \tag{3.6b}$$

$$\partial_z T_{zz} = 0, \tag{3.6c}$$

From (2.2f)–(2.2g), we obtain $\partial_z(v_n + j_s + j_+ + j_-) = 0$ and $\partial_z(j_+ - j_-) = 0$, which we can integrate, imposing the no-flux condition at $z = 0$, to get

$$j_+ = j_-, \tag{3.6d}$$

$$v_n = -j_s - 2j_+. \tag{3.6e}$$

We can use (3.6d) to eliminate the electric potential Φ from the model, which can be obtained by solving

$$\partial_z \Phi = \partial_z \left(\mathcal{G} p + \ln \phi_- - \chi \phi_s \phi_n + \phi_n \right) + \frac{j_+}{\phi_- \mathcal{D}} - \frac{j_s}{\phi_s \mathcal{D}}. \tag{3.7a}$$

The Dirichlet boundary condition for (3.7a) is derived by subtracting (3.3c) and using the definition of the chemical potentials $\mu_\pm$ (see (2.3d)) and is given by

$$\Phi(h(t), t) = \frac{1}{2} \ln \left(\frac{\phi_-}{\phi_+} \right) \Big|_{z=h(t)}. \tag{3.7b}$$

Similarly, we eliminate the pressure from the model by integrating $\partial_z(T_{zz}) = 0$ and applying the boundary condition (3.3a), which leads to

$$p = \frac{\omega^2}{\mathcal{G}} \left[\phi_s \partial_{zz} \phi_s - \frac{(\partial_z \phi_s)^2}{2} \right] + \frac{\left(1 - \phi_n^2\right)}{\phi_n}. \tag{3.8}$$

The evolution of the gel composition is therefore dictated by the two governing equations,

$$\partial_t \phi_s + \partial_z (\phi_s v_n) = -\partial_z j_s, \tag{3.9a}$$

$$\partial_t \phi_+ + \partial_z (\phi_+ v_n) = -\partial_z j_+, \tag{3.9b}$$

which are coupled to the constitutive laws (2.3)

$$j_s = -\frac{\phi_s^2}{1 - \phi_n} \partial_z \mu_s + \frac{2\phi_s}{(1 - \phi_n)\mathcal{D}} j_+, \tag{3.10a}$$

$$j_+ = -\frac{\mathcal{D} \phi_+ \phi_-}{\phi_+ + \phi_-} \partial_z \bar{\mu} + \frac{2\phi_+ \phi_-}{\phi_s (\phi_+ + \phi_-)} j_s, \tag{3.10b}$$

$$v_n = -j_s - 2j_+, \tag{3.10c}$$

$$\bar{\mu} = A(\phi_s, \phi_+) + 2\omega^2 \phi_s \partial_{zz} \phi_s - \omega^2 \left(\partial_z \phi_s \right)^2, \tag{3.10d}$$

$$\mu_s = B(\phi_s, \phi_+) - (1 - \phi_s)\, \omega^2 \partial_{zz} \phi_s - \frac{\omega^2}{2} \left(\partial_z \phi_s \right)^2, \tag{3.10e}$$

$$\phi_n = \frac{1 - \phi_s - 2\phi_+}{1 + \alpha_f}, \tag{3.10f}$$

$$\phi_- = \frac{\phi_+ + (1 - \phi_s - \phi_+)\alpha_f}{1 + \alpha_f}. \tag{3.10g}$$

In (3.10b), $\bar{\mu}$ is defined as the dimensionless chemical potential of the free ions ($\bar{\mu} = \mu_+ + \mu_-$), and (3.10d) is obtained by summing over (2.3d) after nondimensionalization according to the scaling given in (3.4). The functions A, B are defined as follows:

$$\begin{aligned} A(\phi_s, \phi_+) = {} & \ln \left(\phi_+ \frac{\phi_+ + (1 - \phi_s - \phi_+)\alpha_f}{1 + \alpha_f} \right) + 2 \left[1 - \chi \phi_s \right] \frac{1 - \phi_s - 2\phi_+}{1 + \alpha_f} \\ & + \frac{2\mathcal{G}}{1 + \alpha_f} \frac{(1 + \alpha_f)^2 - (1 - \phi_s - 2\phi_+)^2}{1 - \phi_s - 2\phi_+}, \end{aligned} \tag{3.10h}$$

$$\begin{aligned} B(\phi_s, \phi_+) = {} & \ln \phi_s + \left[\chi (1 - \phi_s) + 1 \right] \frac{1 - \phi_s - 2\phi_+}{1 + \alpha_f} \\ & + \frac{\mathcal{G}}{1 + \alpha_f} \frac{(1 + \alpha_f)^2 - (1 - \phi_s - 2\phi_+)^2}{1 - \phi_s - 2\phi_+}. \end{aligned} \tag{3.10i}$$

The system is closed by imposing the boundary conditions:

$$\partial_z \phi_s(h(t),t) = 0, \tag{3.11a}$$

$$\mu_s(h(t),t) = \ln(1-2\phi_0), \tag{3.11b}$$

$$\bar{\mu}(h(t),t) = 2\ln(\phi_0). \tag{3.11c}$$

Here (3.11a)–(3.11b) are the dimensionless counterpart of (3.3b)–(3.3d), while (3.11c) is obtained by summing over the dimensionless form of (3.3c). In one case, Figure 12 (and in Figure SM1 in the supplemental materials (suppmats.pdf [local/web 295KB])), we also consider the scenario in which the gel is isolated from the bath. When this is the case, the boundary conditions (3.11b)–(3.11c) are replaced by no-flux conditions at the free interface (since mobile species are trapped in the gel). Moreover, (3.7b) is replaced with a grounding condition at $z = h(t)$. Hence, for an isolated bath, we impose

$$\partial_z \phi_s(h(t),t) = 0, \tag{3.12a}$$

$$j_s(h(t),t) = j_+(h(t),t) = 0, \tag{3.12b}$$

$$\Phi(h(t),t) = 0. \tag{3.12c}$$

Unless otherwise stated, the parameters used in the simulations are

$$\alpha_f = 0.04,\ \mathcal{D} = 5,\ \chi = 0.78,\ \mathcal{G} = 2\times 10^{-4},\ \omega = 0.025. \tag{3.13a}$$

We further consider the the volume fraction of ions in the bath, ϕ_0, to change at time $t = 0$ from $\phi_{0^-} = 10^{-6}$ to a new value ϕ_{0^+}. For the latter, we consider two scenarios:

$$\text{set 1:}\quad \phi_{0^+} = 10^{-4} \quad \text{and} \quad \text{set 2:}\quad \phi_{0^+} = 10^{-2}. \tag{3.13b}$$

The details on the numerical methods used to solve the system (3.9)–(3.10) in the different scenarios can be found in the supplemental material (suppmats.pdf [local/web 295KB]) section SM2. We note that the rescaled spatial variable which maps the gel to a fixed domain is denoted by $Z = z/h(t) \in [0,1]$.

4. Homogeneous equilibrium states and routes to collapse. We now consider the system (3.9)–(3.10) for ϕ_s and ϕ_+ in equilibrium with an ionic bath. More specifically, we consider homogeneous, flux-free steady states that satisfy the boundary conditions (3.2)–(3.3). The equilibrium states are denoted by (ϕ_s^*, ϕ_+^*) and satisfy

$$A(\phi_s^*, \phi_+^*) - 2\ln(\phi_0) = 0, \tag{4.1a}$$

$$B(\phi_s^*, \phi_+^*) - \ln(1-2\phi_0) = 0. \tag{4.1b}$$

Recall that ϕ_0 denotes the volume fraction of ions in the surrounding bath. The conditions (4.1) define the generalization of the Donnan equilibrium [10] as it applies to our situation, i.e., a polyelectrolyte gel with its fixed charges and the mobile species represented by the salt ions [20].

Considering the shear modulus of the gel $\mathcal{G}$ to be fixed, we investigate how the equilibria depend on the concentration of ions in the bath ϕ_0 and the Flory interaction parameter χ. For large shear moduli $\mathcal{G}$, as in Figure 2(b), there is a unique homogeneous equilibrium solution. Although variations of ϕ_s^* along ϕ_0 are small, there is a sensitive dependence on the Flory interaction parameter χ.

For small $\mathcal{G}$, as in Figure 2(a), there is a range of χ for which the system either exhibits one or three equilibrium states, depending on the value of the salt fraction

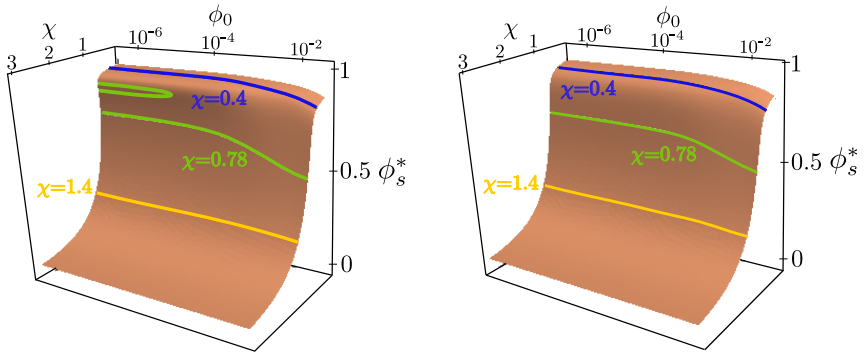

(a) $\mathcal{G} = 2 \times 10^{-4}$. (b) $\mathcal{G} = 10^{-3}$.

FIG. 2. *Surfaces of homogeneous equilibrium solutions for the volume fraction of solvent in the gel ϕ_s^*. The equilibrium solutions are obtained by solving* (4.1) *using the parameter values in* (3.13a). *The surfaces are plotted in terms of the salt fraction in the bath ϕ_0 and the Flory parameter χ. The solid lines represent level sets at fixed values of χ.*

in the bath ϕ_0. A value of $\chi = 0.78$ lies within this range, for example. For large values of ϕ_0, a single equilibrium solution exists that is characterized by a small concentration of solvent; i.e., the equilibrium corresponds to a collapsed state. As ϕ_0 is decreased, a disconnected branch of equilibrium solutions appears. This new branch consists of two highly swollen equilibrium states. The stability of these three equilibria will be characterized in section 6. In summary, the collapsed and most swollen equilibrium states are stable, whereas the state with an intermediate degree of swelling is unstable. A volume phase transition will occur when the gel is driven off the stable swollen branch onto the stable collapsed branch by an increase in ϕ_0.

4.1. Routes to collapse. Our aim is to understand the dynamic response of the gel during the volume phase transition. The analysis in subsequent sections will reveal that the volume phase transition can follow one of two routes, which we summarize in the panels in Figure 3. For the parameter values in (3.13a), the equilibrium solvent fraction is plotted as a function of the salt fraction in the bath ϕ_0 in Figure 3(a). The red square on the swollen branch when $\phi_0 = 10^{-6}$ denotes the initial state of the gel that we consider here.

An example of the first route to the gel collapse occurs when ϕ_0 is increased to 10^{-4}, which we call set 1 in (3.13). In this case, a deswelling front propagates into the gel from the free surface. A snapshot of a numerical simulation, which depicts the propagating front by plotting the solvent fraction as a function of space, is provided in Figure 3(b). Simulation details can be found in section 5. The deswelling front separates two homogeneous states that are not equilibrium solutions. The properties of the front can be predicted from a phase-plane analysis of the steady model (5.3), which will be presented in section 5.1. By exploiting the diluteness of the ions, the steady model (5.3) reduces to a pair of first-order differential equations for the solvent fraction ϕ_s and its gradient $\partial_z \phi_s$ given by (5.9). The deswelling front is well approximated by a heteroclinic orbit that exists in the phase plane of (5.9), shown schematically in Figure 3(c).

An example of the second route to gel collapse occurs when ϕ_0 is increased to 10^{-2}, which we call set 2 in (3.13). In this case, front propagation occurs, but the bulk of the gel undergoes spinodal decomposition, leading to isolated, solvent-poor

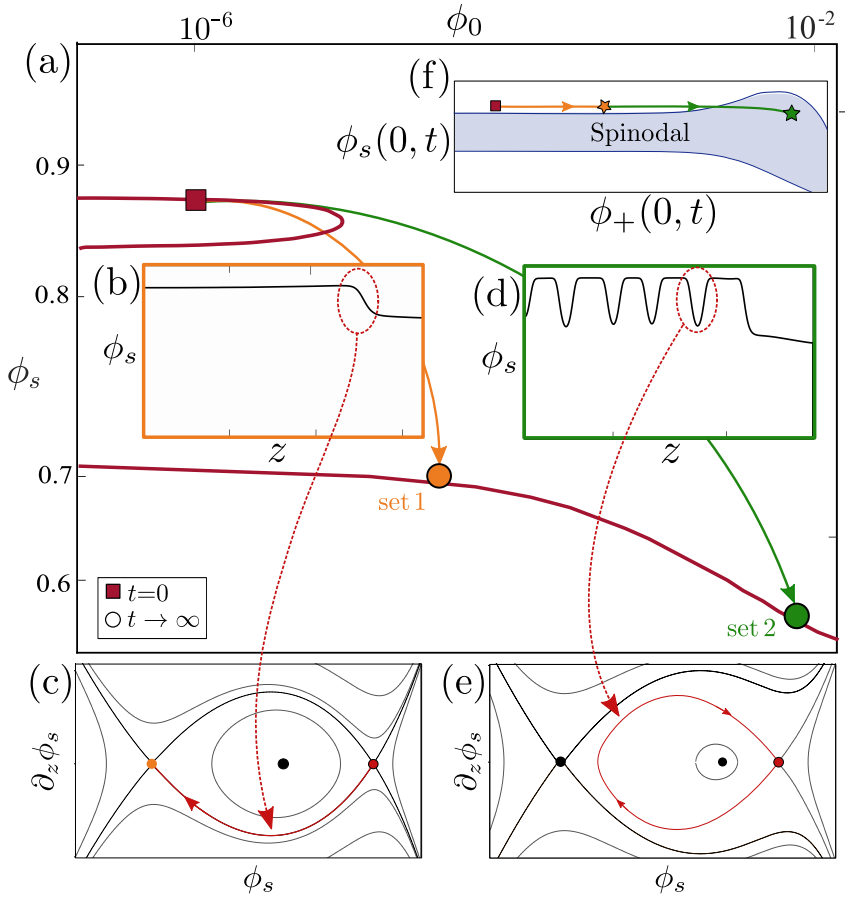

FIG. 3. *Summary of the two routes to collapse.* (a) *Equilibrium solvent fraction obtained by solving* (4.1) *using the parameter values in* (3.13a). *A volume phase transition is triggered by increasing the salt fraction in the bath* ϕ_0 *from* 10^{-6} *(red square) to* 10^{-4} *(set* 1*; orange circle) or* 10^{-2} *(set* 2*; green circle).* (b) *Set* 1 *leads to the first route to collapse, where a deswelling front invades the gel from the free surface, which is seen by plotting the solvent fraction as a function of space; simulation details can be found in section* 5. (c) *A heteroclinic orbit of* (5.9)*, which provides an approximation to the propagating front; see section* 5.1. (d) *The second route to collapse involves front propagation and spinodal decomposition in the bulk of the gel. Simulation details are provided in section* 6.2. (e) *A two-dimensional projection of a homoclinic orbit of* (5.9)*; these orbits provide approximations of the phases that form within the bulk of the gel during the second route to collapse; see section* 6.2. (f) *Evolution of the solvent and cation fraction at the substrate* ($z=0$) *for parameter set* 1 *(orange) and set* 2 *(green). Stars denote the composition after the front has formed. The linearly unstable spinodal regime is shaded and computed in section* 6.1. *For more information about the panels, see section* 4.1. *All panels except* (a) *are to be interpreted schematically.*

phases spontaneously appearing. A snapshot of a numerical simulation (see section 6.2) is provided in Figure 3(d), which shows the solvent fraction as a function of space and the emergence of collapsed phases in the bulk. In section 6.2, we show that the solvent-poor phases are well approximated by homoclinic orbits that exist in the phase space for (5.3). Two-dimensional projections of these orbits are shown schematically in Figure 3(e).

A linear stability analysis of the full time-dependent model, carried out in section 6.1, elucidates why the volume phase transition has two routes. The first route to

collapse occurs when the bulk of the gel has a composition that is linearly stable. That is, the bulk composition remains outside of the linearly unstable region of the phase diagram (this region is called the spinodal region). This is illustrated in Figure 3(f), which tracks how the solvent and cation fraction at the substrate ($z = 0$) evolve during the volume phase transition. The orange star represents the composition after front propagation is initiated. The path that is traced out in the phase diagram avoids the spinodal (shaded) region. The second route to collapse occurs when the bulk of the gel has a composition that is linearly unstable. In this case, the formation of a propagating front pushes the bulk composition into the spinodal region, as shown by the path to the green star in Figure 3(f).

5. Front propagation in a collapsing gel. We start by investigating the simpler scenario of collapse driven uniquely by propagation of a depletion front using numerical simulations of (3.9)–(3.11) with parameter values given by set 1 in (3.13). Results from the numerics are used to generate Figures 4–5. We find that the collapse of the gel is characterized by two timescales: The first is dictated by the fast diffusion of ions into the gel that precede the onset of the depletion front and the second by the slower transport of solvent into the gel. The presence of these two timescales is evident in Figure 4(a), where we illustrate the trajectory the volume fraction ϕ_s and ϕ_+ in the bulk of the gel, specifically, at the substrate ($Z = 0$) in the (ϕ_+, ϕ_s)-plane. As shown in Figure 4(a), for $t \sim O(10^2)$, the ion concentration in the interior of the gel quickly increases while ϕ_s remains approximately constant. As the gel is initially highly swollen, i.e., $\phi_+ \ll \phi_s$, the gel size is determined by the concentration of solvent and so remains approximately constant during this first transient (see Figure 4(c)), i.e., $h(t) \approx h(0)$ for $t \sim O(10^2)$ with $h(0) \approx (1 - \phi_s(0))^{-1} \approx 8$. Focusing on the evolution of ϕ_+ (see Figure 4(b)), we see that within less than one time unit, the concentration builds up at the boundary and subsequently penetrates into the gel. At $t = 12$, the process has almost concluded, and, in fact, early signs of a new front manifest themselves at the free interface, which becomes more pronounced at $t = 301$. Together with the ion concentration, the generalized chemical potential $\bar{\mu}$ move from its initial value $2\ln(\phi_{0^-})$ to approximately $2\ln(\phi_{0^+})$. This difference in chemical potential drives the process of ion diffusion. Since the flux of ions is $\mathcal{D}$ times the gradient of the chemical potential (and the domain size $h(0) \approx 8$), we can estimate the timescale of ionic diffusion as $t \sim [h(0)]^2/[2\mathcal{D}\ln(\phi_{0^+}/\phi_{0^-})] \approx 2.15$, which is consistent

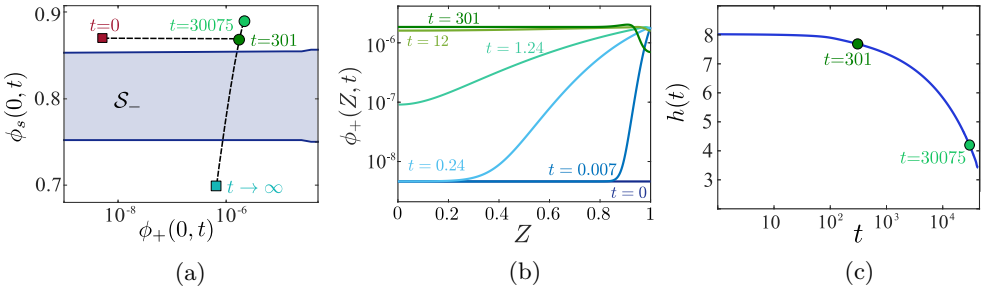

FIG. 4. *Numerical solutions of* (3.9)–(3.11) *for the case of a dilute bath for the parameter set* 1 *in* (3.13). (a) *Evolution of the solution at the substrate (i.e.,* $Z = 0$*) in the* (ϕ_s, ϕ_+) *plane. The instability region* $\mathcal{S}_-$*, defined by* (6.6) *(see stability analysis in section* 6*), is highlighted in blue.* (b) *Evolution of the ion fraction* $\phi_+(Z,t)$. (c) *Time evolution of the size of the gel (color of the dots corresponds to those points used in panel* (a)*).*

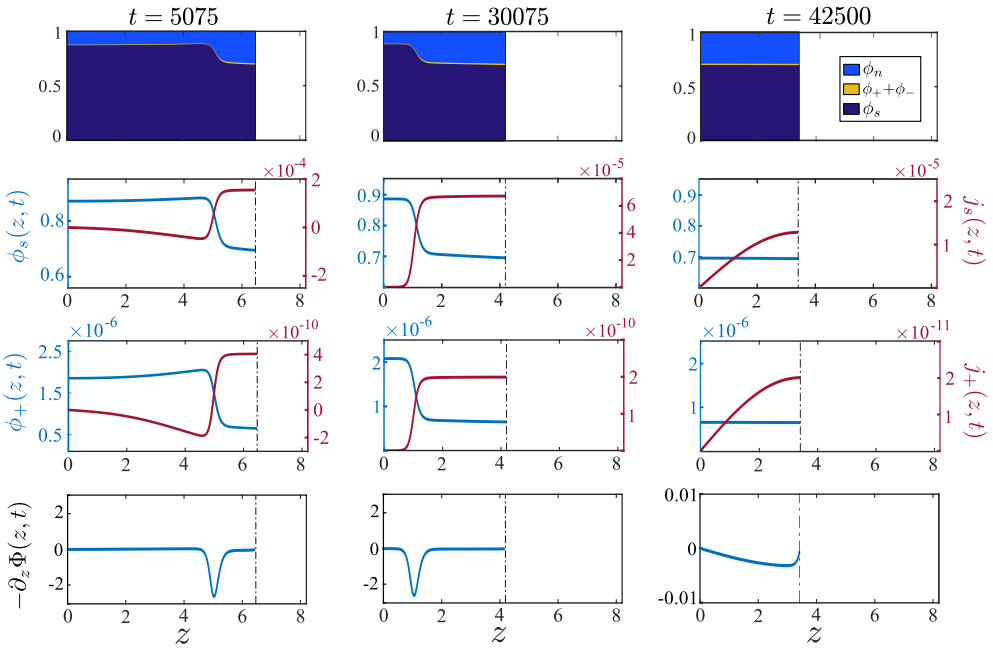

FIG. 5. *Numerical solution of the model* (3.9)–(3.10) *for parameter set* 1 *in* (3.13) *and boundary conditions* (3.11) *(same scenario as Figure* 4*): The first row illustrates the gel composition at different points in time. For the same time points, we also plot the volume fractions, the corresponding fluxes, and the electric field* $-\partial_z\Phi$ *(defined by using* (3.7a)*).*

with the observation in the numerical simulations. Using a scaling argument, we can also estimate the concentration of ions in the gel prior to and after the transient. Given that the concentration of ions in the bath is small, i.e., $\phi_0 \ll 1$, the logarithmic term $\ln\phi_0$ in (4.1a) becomes large and needs to be balanced. Since the gel is not too swollen, i.e., $1-\phi_s-2\phi_+ \gg \phi_0$, or dry, i.e., $\phi_n^{-1}\mathcal{G} \ll 1$, the only term in (3.10h) that can balance $\ln\phi_0$ is the logarithmic term so that

$$\phi_+ \frac{\phi_+ + \alpha_f(1-\phi_s-\phi_+)}{1+\alpha_f} \sim {\phi_{0^+}}^2, \tag{5.1}$$

and given the chosen value of α_f (see 3.13)), the balance (5.1) gives

$$\phi_+ \sim {\phi_{0^+}}^2(1-\phi_s)^{-1}/\alpha_f \tag{5.2}$$

so that we predict the concentration of ions to be $\phi_+ \sim 1.25\times10^{-10}$ prior to $t=0$ and $\phi_+ \sim 1.25\times10^{-6}$ after the fast ion diffusion (given $(1-\phi_s)^{-1}\approx 8$). These are in good agreement with numerical result in Figure 4(b).

After the ion concentration has equilibrated, a slower process takes place whereby solvent is removed from the gel through the aforementioned depletion front. This is illustrated in Figure 5, where we present snapshots in time of the gel composition (see first row). For the same time points of the snapshots, we also illustrate the values of the volume fractions, fluxes, and electric field in the gel. The front is clearly seen in the concentration profiles for the solvent ϕ_s as well as for the mobile ion species ϕ_+ and the gradient of the electric potential $-\partial_z\Phi$, i.e., the electric field in the gel. In the poorly swollen region of the gel (near the free interface), $\phi_s \approx 0.7$; using the scaling

(5.2), we therefore expect a reduction in the concentration of ions, More precisely, we obtain $\phi_+ \sim 8 \times 10^{-7}$, which is again in line with the numerical results. In the last column ($t = 42500$), the front has reached the substrate, and the gel has collapsed with its composition having reached a new state (see "powder" blue square in Figure 4(a)). The solvent flux j_s is only on the order of 10^{-4}; hence, the appropriate timescale for the depletion front movement is $O(10^4)$. The main contribution is from the gradient of the chemical potential μ_s, which is set by the function B (see (3.10i)). The latter is connected with $\mathcal{G}$, which is small, and it is this small value that determines the slow collapse.

To summarize (as illustrated in Figure 4(a)), the gel starts from a state of high concentration of solvent and a small concentration of co-ions. From there, it quickly evolves to a new state with higher salt content. As derived in section 6 and shown in Figure 4(a), both of these states are stable and show no sign of spinodal decomposition. Instead, a depletion front moves through the gel. At a later time (i.e., $t \sim 30000$), as the front approaches the substrate, the solvent concentration $\phi_s(0,t)$ increases slightly before decreasing to its new linearly stable steady-state value, with a slightly higher salt but a much lower solvent concentration.

5.1. Phase-plane analysis. The slow movement of the depletion fronts on the diffusive timescale suggests that these structures are in a quasi-stationary state, which simplifies their analysis by enabling the time derivatives and fluxes from the system (3.9)–(3.10) to be neglected so that the solution will only depend on the spatial variable z. Since fluxes are negligible, μ_s, $\bar{\mu}$ are almost constant (independent of z) in an $O(1)$ vicinity of the front. With this assumption and after rescaling z with ω, we have

$$\partial_z \phi_s = q, \tag{5.3a}$$

$$\partial_z q = \frac{1}{1-\phi_s}\left[B(\phi_s,\phi_+) - \mu_s\right] - \frac{1}{2(1-\phi_s)} q^2, \tag{5.3b}$$

$$\mu_s = \frac{\phi_s - 1}{2\phi_s}\left[\bar{\mu} - A(\phi_s,\phi_+)\right] + B(\phi_s,\phi_+) - \frac{1}{2\phi_s} q^2, \tag{5.3c}$$

where A and B are as defined by (3.10h)–(3.10i) and we introduce the auxiliary variable q. The fixed points $(q,\phi_s,\phi_+) = (0,\phi_s^0,\phi_+^0)$ of the system (which correspond to homogeneous equilibrium states for the full model) are found from (5.3) via

$$A(\phi_s^0,\phi_+^0) = \bar{\mu}, \quad B(\phi_s^0,\phi_+^0) = \mu_s. \tag{5.4}$$

As shown in Figure 6, the number of fixed points varies depending on the values assigned to μ_s and $\bar{\mu}$. For sufficiently small values of μ_s (see $\mu_s = -0.1$, for example), the system has a unique fixed point. As we increase the value of μ_s, there is an intermediate region near $\mu_s = 0$ where multiple fixed points can exist depending on the values of $\bar{\mu}$. As shown on the right-hand side panel of Figure 6, when considering $\mu_s = 10^{-4}$, the system has three fixed points when $\bar{\mu}$ is below a critical negative value, i.e., in the dilute limit $\phi_+^0 \ll 1$. As $\bar{\mu}$ increases, the system undergoes a saddle-node bifurcation resulting in a unique fixed point. Note that the equilibrium states computed in section 4 are a subset of the fixed points of the system (5.3), as the values of μ_s and $\bar{\mu}$ are not independent, being set by the ionic bath via the boundary conditions (3.11b)–(3.11c).

For our local analysis, we note that the depletion front represents a narrow, slowly moving transition between two almost homogeneous states so that we can approximate

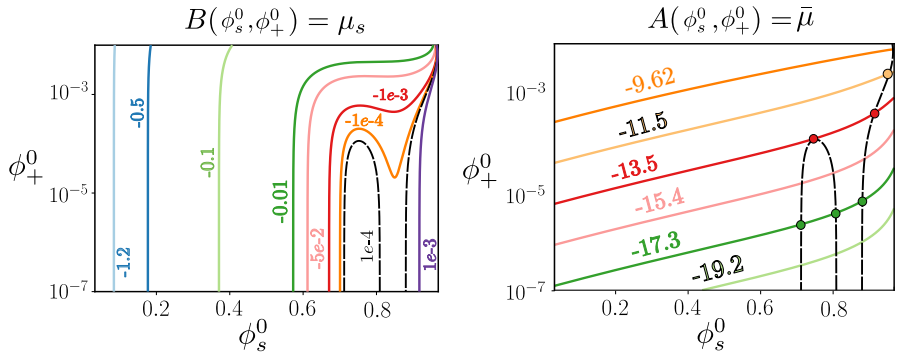

FIG. 6. *Level sets for the functions A and B (defined by* (3.10h)–(3.10i)*) that define the fixed points of the system* (5.3)*. Note that the functions are expressed in terms of ϕ_s^0 and ϕ_+^0. The dashed line in right panel is taken from the left one (i.e., $\mu_s \equiv 10^{-4}$). The value of the parameters χ, α_f and $\mathcal{G}$ are given in* (3.13a).

it by a quasi-stationary solution that tends to homogeneous states as $z \to \pm\infty$. We then linearize around $(0, \phi_s^0, \phi_+^0)$ and determine the number of modes consistent with these limits, which we then use to carry out a degree-of-freedom count. We make the ansatz

$$\phi_s = \phi_s^0 + \delta\phi_s^1 \mathrm{e}^{sz}, \quad q = \delta q^1 \mathrm{e}^{sz}, \quad \phi_+ = \phi_+^0 + \delta\phi_+^1 \mathrm{e}^{sz}, \tag{5.5}$$

with $\delta \ll 1$ and s being a constant. Inserting this, we obtain at $O(\delta)$ the condition

$$\begin{bmatrix} B_{\phi_s} - (1-\phi_s^0)s^2 & B_{\phi_+} \\ (1-\phi_s^0)A_{\phi_s} + 2\phi_s^0 B_{\phi_s} & (1-\phi_s^0)A_{\phi_+} + 2\phi_s^0 B_{\phi_+} \end{bmatrix} \begin{bmatrix} \phi_s^0 \\ \phi_+^0 \end{bmatrix} = 0, \tag{5.6}$$

where the subscripts ϕ_s and ϕ_+ denote partial derivatives of A and B, which are evaluated at the equilibrium point (ϕ_s^0, ϕ_+^0). In order for the system to have nontrivial solutions, we must set the determinant of the coefficient matrix to zero, which gives

$$s^2 = \frac{A_{\phi_+} B_{\phi_s} - A_{\phi_s} B_{\phi_+}}{(1-\phi_s^0)\, A_{\phi_+} + 2\phi_s^0\, B_{\phi_+}}. \tag{5.7}$$

We therefore conclude that the equilibrium is a saddle point if $s^2 > 0$. We now seek a nonhomogeneous quasi-stationary solution connecting two saddle points, $(0, \phi_s^a, \phi_+^a)$ and $(0, \phi_s^b, \phi_+^b)$. This corresponds to imposing the far-field conditions $(\phi_s, \phi_+) \to (\phi_s^a, \phi_+^a)$ and $(\phi_s, \phi_+) \to (\phi_s^b, \phi_+^b)$ as $z \to -\infty$ and $z \to +\infty$, respectively. When considering the degrees of freedom in the solution, we have one mode for each saddle point, which is consistent with the limit, namely, $s^a < 0$ for $(0, \phi_s^a, \phi_+^a)$ and $s^b > 0$ for $(0, \phi_s^b, \phi_+^b)$. These account for two degrees of freedom, which, together with the two unknown constants μ_s and $\bar{\mu}$, add up to four degrees of freedom. The system (5.3) is second order and hence removes two degrees of freedom, and the invariance of any solution with respect to translations along the z-axis subtracts another one. Hence, one degree of freedom remains, and this is associated with $\bar{\mu}$, which needs to be given. We note that a full expansion at higher orders about the quasi-stationary solution might lead to additional constraints that fix the degree of freedom remaining in the system. However, this goes beyond the purpose of this analysis, which aims at understanding the structure of the depletion front.

5.1.1. The limit of dilute salt concentrations. We here consider the limit of dilute salt concentration, i.e., $\phi_+ \ll \phi_s < 1$, which is representative of the numerical results from Figure 5. Here, we use the same equations and boundary conditions and the same parameter set, where ϕ_+ is small. Inspired by the scaling (5.2), we rescale the model variables via

$$\phi_+ = \alpha_f \epsilon^2 \tilde{\phi}_+, \quad \bar{\mu} = 2\ln(\alpha_f \epsilon) + \tilde{\mu}, \tag{5.8}$$

where the dilute limit is therefore taken by considering $\epsilon \to 0$. Note that if we define $\epsilon = \phi_{0^+}/\alpha_f$, we recover (5.2) up to a factor $1-\phi_s$, allowing us to relate the phase-plane analysis to the numerical simulations in the presence of a bath (which is instead here neglected). Substituting (5.8) into (5.3) and considering only the leading order problem in this limit, we obtain

$$\partial_z \phi_s = q, \tag{5.9a}$$

$$\partial_z q = \frac{1}{1-\phi_s}\left[B_0(\phi_s) - \mu_s\right] - \frac{1}{2(1-\phi_s)} q^2, \tag{5.9b}$$

$$\mu_s = \frac{1-\phi_s}{2\phi_s}\left[A_0(\phi_s, \tilde{\phi}_+) - \tilde{\mu}\right] + B_0(\phi_s) - \frac{1}{2\phi_s} q^2, \tag{5.9c}$$

with

$$A_0(\phi_s, \tilde{\phi}_+) = \ln\left[\left(\frac{1-\phi_s}{1+\alpha_f}\right)\frac{\tilde{\phi}_+}{\phi_s^2}\right] - 2\chi\left(\frac{1-\phi_s}{1+\alpha_f}\right) + 2B_0(\phi_s), \tag{5.9d}$$

$$B_0(\phi_s) = \ln(\phi_s) + (\chi(1-\phi_s)+1)\left(\frac{1-\phi_s}{1+\alpha_f}\right) + \mathcal{G}\frac{(1+\alpha_f)^2 - (1-\phi_s)^2}{(1+\alpha_f)(1-\phi_s)}. \tag{5.9e}$$

Equations (5.9a) and (5.9b) decouple from the algebraic constraint (5.9c). The first integral of (5.9a) and (5.9b) is then used to investigate the phase plane as a function of the chemical potential μ_s as illustrated in Figure 7. In contrast to a nonionic hydrogel [15], the contribution of the fixed charges allows multiple fixed points to exist when $\mu_s = 0$, i.e., for a gel in contact with pure water. There is a unique critical value of μ_s, denoted by μ_s^c, for which the two saddle points are connected by an heteroclinic orbit, corresponding to a front-type nonhomogeneous quasi-stationary solution (see Figure 7(b)). If $\mu_s < \mu_s^c$ as shown in Figure 7(a), there is a homoclinic orbit attached to the right fixed point (i.e., the orange point), corresponding to a quasi-stationary solution with a localized solvent-depleted zone. On the contrary, for $\mu_s > \mu_s^c$, the homoclinic orbit is attached to the left fixed point (i.e., the blue point; see Figure 7(c)), which represents a localized solvent-rich zone. We can find the critical value of μ_s by combining (5.9a) and (5.9b) into a second-order equation and using $f = 1/\sqrt{1-\phi_s}$ as an integrating factor to obtain

$$\int_{\phi_s^a}^{\phi_s^b} \frac{B_0(\phi_s) - \mu_s}{(1-\phi_s)^2} \mathrm{d}\phi = 0, \tag{5.10a}$$

$$B_0(\phi_s^a) - \mu_s = 0, \quad B_0(\phi_s^b) - \mu_s = 0, \tag{5.10b}$$

where ϕ_s^a and ϕ_s^b are the values of the solvent fraction at the two saddle points. Note that this is a Maxwell condition for the coexisting states ϕ_s^a and ϕ_s^b, which are independent of the ion fraction $\tilde{\phi}_+$ in the dilute limit. Solving numerically the system with the parameters for α and χ and $\mathcal{G}$ corresponding parameter set 1 in (3.13) gives

$$\mu_s = 0.903 \times 10^{-4}, \quad \phi_s^a = 0.883, \quad \phi_s^b = 0.710. \tag{5.11}$$

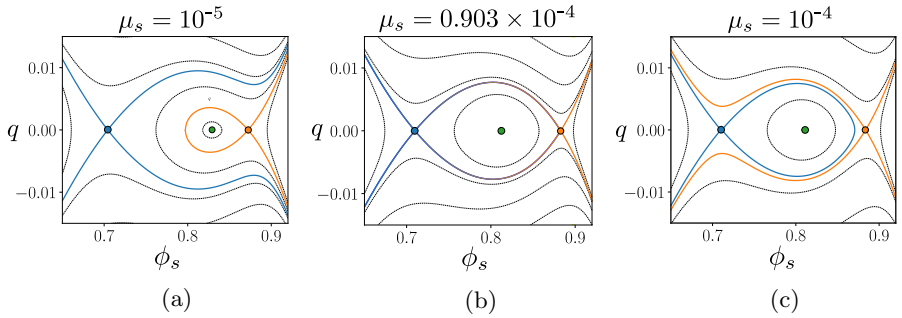

FIG. 7. *Phase-plane analysis for the dilute limit (i.e.,* (5.9a) *and* (5.9b)*) with parameters as in* (3.13a) *and three different values of* μ_s*:* (a) $\mu_s < \mu_s^{(c)}$; (b) $\mu_s = \mu_s^{(c)}$ *for which there is an heteroclinic orbit connecting the two equilibrium state;* (c) $\mu_s > \mu_s^c$. *Fixed points are highlighted by small circles, trajectories leaving from or asymptoting into fixed points are indicated by solid colored lines, while all other trajectories are denoted by dashed black lines.*

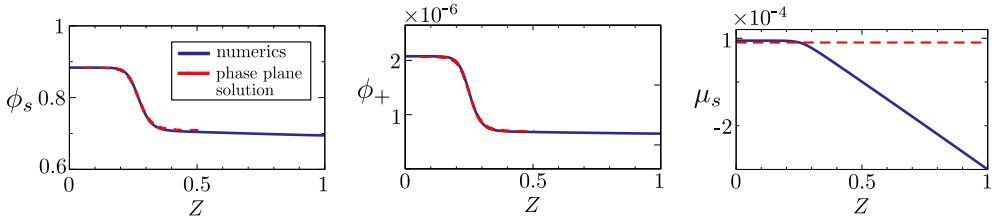

FIG. 8. *Comparison of the asymptotic approximation for the phase-plane solution* (5.9)–(5.10) *(shown with dashed red lines) for* ϕ_s, ϕ_+, *and* μ_s *with the numerical results from Figure* 5 *at a time* $t = 30075$ *when the concentration profile fronts have settled into a quasistationary state (solid black lines), using the parameter set* 1 *in* (3.13). *A single shift along the* Z*-axis was applied to all phase-plane profiles so that* ϕ_s *matches the numerical solution at* $\phi_s = 0.8$.

As shown in Figure 8, the phase-plane analysis is overall in good agreement with the dynamical simulation from Figure 5. While the value of μ_s at the free interface (i.e., $Z = 1$) is set by the bath, in the bulk of the gel, μ_s sets around the critical value obtained by our phase-plane analysis (see (5.11)). Note that provided $\tilde{\mu}$ is known from the numerical simulations, we can use the constraint (5.9c) to compute $\tilde{\phi}_+$. In this set of simulations, we find $\tilde{\mu} \in (2.75 \times 10^{-8}, 3.89 \times 10^{-4})$, that is, $\tilde{\mu} \ll \ln(\epsilon\alpha_f)$, and therefore (see (5.8)) we have set it to zero for the phase-plane solutions involving parameter set 1.

5.1.2. The general case. We now explore the nondilute limit. This requires solving the general case of (5.3)–(5.4), which is done numerically applying a shooting method. Starting from slightly perturbed values for the left state, we integrate the resulting initial value problem for a system of differential algebraic equations (DAEs), rewritten in terms of ϕ_s and ϕ_+ as the dependent variables. For a fixed the value of $\tilde{\mu}$, there is a unique value of μ_s such that the trajectory connects to the right equilibrium. The critical value of μ_s is then determined using a bisection iteration. The resulting solution defines μ_s and the associated values for the left and right state ϕ_s^a and ϕ_s^b for ϕ_s and similarly for ϕ_-.

For the case of $\tilde{\mu}$ equal to zero, the results are shown in Figure 9. The plots in (a) show graphs of the values for $100\mu_s$ and for the values of the two equilibrium states for ϕ_s^0 and $\tilde{\phi}_+^0$ as a function of $\phi_{0^+} = \alpha_f \epsilon$ (5.10). Moreover, near to $\epsilon = 0$, the

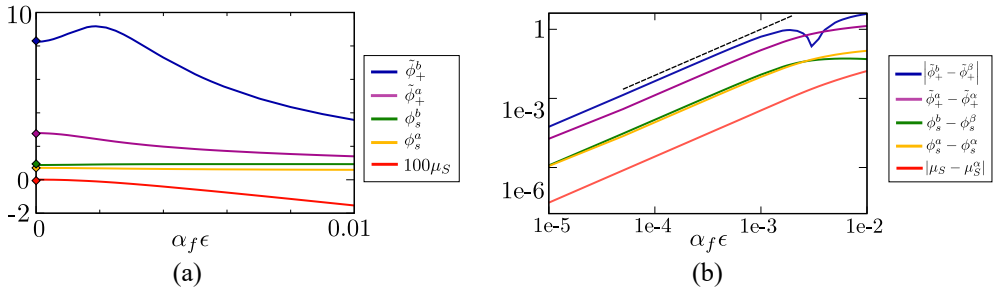

FIG. 9. (a) *The figure shows graphs of* $100\mu_s$, ϕ_s^a, ϕ_s^b, $\tilde{\phi}_+^a$, *and* $\tilde{\phi}_+^b$, *listed in order from bottom to top. The diamonds at* $\epsilon = 0$ *represent the values* $100\mu^\alpha$, ϕ_s^α, ϕ_s^β, $\tilde{\phi}_+^\alpha$, *and* $\tilde{\phi}_+^\beta$ *obtained from the asymptotic solution as given by* (5.11) *and* (5.9c). (b) *This log-log plot has graphs for* $|\mu_s - \mu_s^\alpha|$, $\phi_s^a - \phi_s^\alpha$, $\phi_s^b - \phi_s^\beta$, $\tilde{\phi}_+^a - \tilde{\phi}_+^\alpha$, $|\tilde{\phi}_+^b - \tilde{\phi}_+^\beta|$. *The short top line represents a quadratic function and is included to guide the eye.*

behavior is quadratic, as can be seen from the log-log plot in Figure 9(b), consistent with neglecting $O(\epsilon^2)$-terms in (5.9). However, for $\alpha_f\epsilon$ greater than 1×10^{-3}, the value for $\tilde{\phi}_{+,2}$ departs from this behavior and in fact passes through a maximum as it reverses its trend. We remark that μ_s is positive for $\alpha_f\epsilon \leq 5.45 \times 10^{-3}$ and negative for larger values of ϵ.

A comparison between DAE solutions and the PDE simulation where the dilute approximation is no longer valid will be carried out in section 6.2. There, we show that the estimates from the phase space analysis for the DAE system (5.3)–(5.4) can be used to investigate the structure observed in Figure 3 (set 2). In addition, for parameter set 1, a comparison of the results from the DAE system (5.3)–(5.4) and the PDE simulations is given in the supplemental notes, section SM4.

6. Spinodal decomposition. In the previous section, we have seen how changing the properties of the bath can be sufficient to induce phase separation of the gel via development and propagation of a depletion front. In this section, we are interested in another common modality of phase separation: spinodal decomposition. In this scenario, a spatially homogeneous region of the gel spontaneously separates into regions of high and low solvent content once perturbed with noise. This can occur when the homogeneous state the gel is in is unstable. As discussed in [15], spinodal decomposition can be induced in neutral gels by changing the temperature T and hence the parameter χ. While we will also discuss this scenario briefly (see Figure 12), for the polyelectrolyte gels studied here, we examine whether spinodal decomposition can also be induced by changing the ion concentration in the bath.

6.1. Stability analysis. As shown in Figure 3, the transition between different equilibrium states can also be accompanied by phase separation via spinodal decomposition of the gel bulk (region ahead of the front). To understand this mechanism, we investigate the stability of the initial homogeneous composition of the gel bulk, here denoted by $(\bar{\phi}_s, \bar{\phi}_+)$, to small amplitude perturbations. As in section 5.1, we rescale z with ω, which is the characteristic length scale of the internal interfaces; to ease the algebra, we further scale t with ω^{-1}. Since ω is small, the homogeneous region of the gel now fills the entire space $-\infty < z < \infty$.

We can now perturb the base state $(\bar{\phi}_s, \bar{\phi}_+)$ with normal modes suitable for an infinite domain by letting

$$\phi_s = \bar{\phi}_s + \delta\tilde{\phi}_s e^{ikz+\lambda t}, \quad \phi_+ = \bar{\phi}_+ + \delta\tilde{\phi}_+ e^{ikz+\lambda t} \tag{6.1}$$

with $k \in \mathbb{R}$, $\delta \ll 1$, and $\lambda \in \mathbb{C}$ being the wavenumber, amplitude, and growth rate of the perturbation. Substituting (6.1) into the governing equations (3.9)–(3.10) and keeping only the $O(\delta)$ terms leads to the 2×2 system

$$\lambda\tilde{\phi}_s + k^2\left[\left(1-\bar{\phi}_s\right)\tilde{j}_s - 2\bar{\phi}_s\tilde{j}_+\right] = 0, \tag{6.2a}$$

$$\lambda\tilde{\phi}_+ + k^2\left[\left(1-2\bar{\phi}_+\right)\tilde{j}_+ - \bar{\phi}_+\tilde{j}_s\right] = 0, \tag{6.2b}$$

where $\tilde{j}_s$ and $\tilde{j}_+$ are the solution of the linear system

$$\left(1+\frac{\alpha_f\bar{\phi}_n}{\mathcal{D}\bar{\phi}_s}\right)\tilde{j}_s - \frac{\alpha_f\bar{\phi}_n}{\mathcal{D}\bar{\phi}_-}\tilde{j}_+ = \Big[\left(\bar{\phi}_s B_{\phi_+} + \bar{\phi}_+ A_{\phi_+}\right)\tilde{\phi}_+ + \left(k^2\bar{\phi}_s\left(1+\alpha_f\right)\bar{\phi}_n + \bar{\phi}_s B_{\phi_s} + \bar{\phi}_+ A_{\phi_s}\right)\tilde{\phi}_s\Big] \tag{6.2c}$$

$$\left(1+\frac{\bar{\phi}_+}{\bar{\phi}_-}\right)\tilde{j}_+ - \frac{2\bar{\phi}_+}{\bar{\phi}_s}\tilde{j}_s = \mathcal{D}\bar{\phi}_+\left[\left(A_{\phi_+} - 2k^2\bar{\phi}_s\right)\tilde{\phi}_s + A_{\phi_+}\tilde{\phi}_+\right]. \tag{6.2d}$$

The subscripts ϕ_s, ϕ_+ now denote the derivatives of A and B with respect to these variables evaluated at $(\bar{\phi}_s, \bar{\phi}_+)$. The values of $\bar{\phi}_-$ and $\bar{\phi}_n$ are defined by evaluating (3.10f)–(3.10g) at $\bar{\phi}_s, \bar{\phi}_+$. Note that we could have solved explicitly for $\tilde{j}_s$ and $\tilde{j}_+$, but this would not benefit the exposition given the complexity of the equations. Imposing that the system (6.2) has nontrivial solution, we obtain the growth rate $\lambda = \lambda(k)$ as the roots of the characteristic polynomial,

$$P_k(\lambda) = \lambda^2 + \frac{\zeta_{20} + \zeta_{22}k^2}{\zeta_1}k^2\lambda + \frac{\zeta_{30} + \zeta_{32}k^2}{\zeta_1}k^4\mathcal{D}, \tag{6.3}$$

where the relevant coefficients ζ are functions of $(\bar{\phi}_s, \bar{\phi}_+)$ (see supplemental material (suppmats.pdf [local/web 295KB]), section SM3) and $\zeta_1 > 0$. The two roots of (6.3) are

$$\lambda_\pm(k) = \frac{1}{2}\left[\mathcal{T}_k \pm \sqrt{\mathcal{T}_k^2 - 4\Delta_k}\right], \tag{6.4a}$$

$$\mathcal{T}_k = -\frac{\zeta_{20} + \zeta_{22}k^2}{\zeta_1}k^2, \quad \Delta_k = \frac{\zeta_{30} + \zeta_{32}k^2}{\zeta_1}k^4\mathcal{D}. \tag{6.4b}$$

The homogeneous state is stable if and only if the real part of $\lambda_\pm(k)$ is negative for all k. We note that $\lambda_\pm(k)$ are equivalent to the eigenvalues of the linear dynamical system $\dot{\boldsymbol{y}} = A_k\boldsymbol{y}$, where $\boldsymbol{y} \in \mathbb{R}^2$ and $A_k \in \mathbb{R}^{2\times 2}$ has trace $\mathcal{T}_k$ and determinant Δ_k. We will refer to this class of dynamical systems, which is parametrized by k, as Σ_k. The problem of studying the stability of the mode k is therefore analogous to studying the stability of $(0,0)$ for the system Σ_k. We therefore have that the kth mode is stable if and only if $\mathcal{T}_k < 0$ and $\Delta_k > 0$. When considering $k \gg 1$, $\Delta_k \approx \mathcal{D}k^6\zeta_{32}/\zeta_1$ and $\mathcal{T}_k \approx -\zeta_{22}k^4/\zeta_1$. Since ζ_1, ζ_{22}, and ζ_{32} are always positive, the conditions of stability are always satisfied for large wavenumbers. This implies that $(\bar{\phi}_s, \bar{\phi}_+)$ is unstable if and only if the system Σ_k has at least a bifurcation point $k_* > 0$, where the stability of $\boldsymbol{y} = (0,0)$ changes. If Σ_k has no bifurcation point, then $(\bar{\phi}_s, \bar{\phi}_+)$ is stable. Let us assume such $k_* > 0$ exist. Then

$$\text{either} \quad \Delta_{k_*} = 0 \text{ and } \mathcal{T}_{k_*} \le 0 \tag{6.5a}$$

$$\text{or} \quad \Delta_{k_*} \ge 0 \text{ and } \mathcal{T}_{k_*} = 0, \tag{6.5b}$$

where (6.5a) corresponds to $(0,0)$ switching from a saddle to a stable node, while (6.5a) corresponds to a transition from an unstable to a stable spiral. The first scenario can

occur only if $\zeta_{30} < 0$ and $\zeta_{30}\zeta_{22} - \zeta_{20}\zeta_{32} \leq 0$ (condition 1), while the second can occur only if $\zeta_{20} < 0$ and $\zeta_{30}\zeta_{22} - \zeta_{20}\zeta_{32} \geq 0$ (condition 2). If we denote by $\mathcal{S}_-$ the set of unstable homogeneous states, this is given by the union of the subsets of states satisfying condition 1 or 2. Manipulating the given inequalities, we find that the condition on $\zeta_{30}\zeta_{22} - \zeta_{20}\zeta_{32}$ does not actually play a role in determining the stability of a homogeneous state and $\mathcal{S}_-$ is given by

$$\mathcal{S}_- = \left\{(\bar{\phi}_s, \bar{\phi}_+) \in (0,1)^2 \text{ s.t. } \zeta_{30}(\bar{\phi}_s, \bar{\phi}_+) < 0 \text{ or } \zeta_{20}(\bar{\phi}_s, \bar{\phi}_+) < 0\right\}. \tag{6.6}$$

The spinodal curve, which delimits the region of stability, is therefore

$$\begin{aligned} \partial\mathcal{S} = &\left\{(\bar{\phi}_s, \bar{\phi}_+) \in (0,1)^2 \text{ s.t. } \zeta_{30}(\bar{\phi}_s, \bar{\phi}_+) = 0 \,\&\, \zeta_{20}(\bar{\phi}_s, \bar{\phi}_+) \geq 0\right\} \\ &\bigcup \left\{(\bar{\phi}_s, \bar{\phi}_+) \in (0,1)^2 \text{ s.t. } \zeta_{30}(\bar{\phi}_s, \bar{\phi}_+) \geq 0 \,\&\, \zeta_{20}(\bar{\phi}_s, \bar{\phi}_+) = 0\right\}. \end{aligned} \tag{6.7}$$

6.1.1. The limit of dilute salt concentration. Let us define $\bar{\phi}_+ = \alpha_f \epsilon^2 \tilde{\phi}_+$ (as in section 5.1) and take the limit $\epsilon \to 0$. Reasoning as in the previous section (more details are in section SM3.1 of supplemental material (suppmats.pdf [local/web 295KB])), we obtain that the stability of the system is governed by the leading order approximation of the coefficients $\zeta_{20}^{(0)}$ and $\zeta_{30}^{(0)}$, which are of the form

$$\zeta_{20}^{(0)} = \frac{(\bar{\phi}_n^{(0)})^{-1}}{1+\alpha_f}\left(B_{\phi_s}^{(0)}\bar{\phi}_s(1-\bar{\phi}_s) + \left[\mathcal{D} + \alpha_f \bar{\phi}_s^{-1}\bar{\phi}_n^{(0)}\right]\right), \quad \zeta_{30}^{(0)} = \bar{\phi}_s B_{\phi_s}^{(0)}, \tag{6.8}$$

where $B_{\phi_s}^{(0)} = B_{\phi_s}^{(0)}(\bar{\phi}_s)$ only depends on the concentration of the solvent. It is therefore apparent that when $\zeta_{20}^{(0)} = 0$, $\zeta_{30}^{(0)} < 0$, while whenever $\zeta_{30}^{(0)} = 0$, $\zeta_{20}^{(0)} > 0$. Consequently, the spinoidal curve $\partial\mathcal{S}$ as in (6.7) reduces to

$$\partial\mathcal{S} = \left\{\bar{\phi}_s \in (0,1) \text{ s.t. } B_{\phi_s}^{(0)}(\bar{\phi}_s) = 0\right\}, \tag{6.9a}$$

where

$$B_{\phi_s}^{(0)}(\bar{\phi}_s) = \bar{\phi}_s^{-1} - \frac{\left[1 + 2\chi(1-\bar{\phi}_s)\right]}{1+\alpha_f} + \frac{\mathcal{G}}{1+\alpha_f}\left[1 + \left(\frac{1+\alpha_f}{1-\bar{\phi}_s}\right)^2\right]. \tag{6.9b}$$

As discussed in the supplemental material (suppmats.pdf [local/web 295KB]), section SM3.1, (6.9) still holds for $\alpha_f \to 0$. Furthermore, setting $\alpha_f = 0$, we retrieve the same result as in [15] for phase separation in neutral hydrogels (i.e., gel with no fixed charge on the polymer network). As shown in Figure 10(a), as we increase α_f, the domain $\mathcal{S}_-$ shrinks, which means that a higher concentration of fixed charges on the polymer network can stabilize the system. Small perturbations of the homogeneous state will generate an electric field that tends to redistribute charges homogeneously. As the number of fixed charges in the network increases, so does the strength of the electric field, resulting in the stabilization of homogeneous states. As shown in Figure 10(b), we can see a similar trend also for the nondilute limit (more details in the following section). Fixed charges tend again to stabilize the system; however, for larger $\bar{\phi}_+$, the shrinking of the unstable region $\mathcal{S}_-$ is less than in the dilute scenario.

6.1.2. The general case. Let us now go back to the general case of a nondilute solutions. For the reference parameter values in (3.13), we have that $\zeta_{20}(\bar{\phi}_s, \bar{\phi}_+)$ is always positive. This implies that the transition to instability can only occur via a

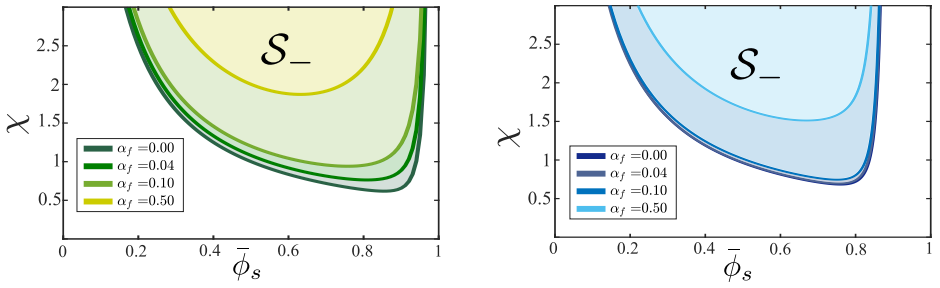

(a) (b)

FIG. 10. *Effect of the fixed charges on the stability region of an homogeneous steady state for* (a) *dilute salt solution* (b) *nondilute solution* ($\bar{\phi}_+ = 0.05$). *We highlight with color the instability region* $\mathcal{S}_-$, *which is the region contained in the curve* ∂S. *In both plots,* $\mathcal{G}$ *is set to its default given in* (3.13a).

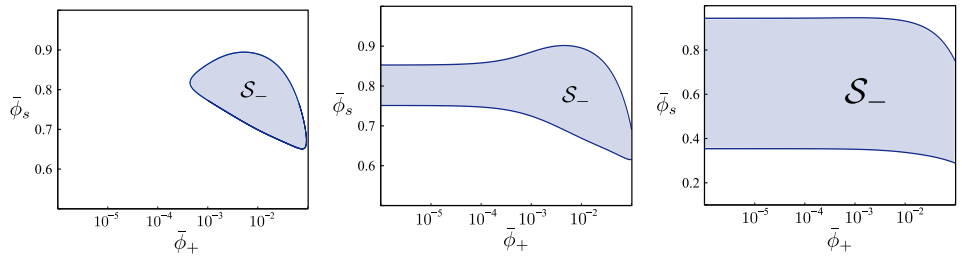

(a) $\chi = 0.75$. (b) $\chi = 0.78$. (c) $\chi = 1.5$.

FIG. 11. *Plots of the instability region* $\mathcal{S}_-$ *(as defined by* (6.6)*) for increasing values of* χ. *Parameters* α_f *and* $\mathcal{G}$ *are set to their default given in* (3.13a).

saddle-node bifurcation. Hence, $\partial\mathcal{S}$ is implicitly defined by $\zeta_{30}(\bar{\phi}_s, \bar{\phi}_+) = 0$, which can be computed via numerical continuation.

As shown in Figure 11, for concentrations $\bar{\phi}_+ < 10^{-4}$, the shape and size of the domain $\mathcal{S}_-$ is independent of the actual value of $\bar{\phi}_+$, in line with the result from the dilute analysis in section 5.1. As we move away from the dilute limit by increasing $\bar{\phi}_+$, two scenarios are possible. If χ is sufficiently small (as in Figure 11(a)–11(b)), then the size of $\mathcal{S}_-$ tends to increase with $\bar{\phi}_+$. This is particularly evident in Figure 11(a), where in the dilute regime all homogeneous states are stable, and the system only allows for spinodal decomposition to occur in the nondilute regime, i.e., $\bar{\phi}_+ \approx 10^{-3}$. If we are, however, to increase $\bar{\phi}_+$ further (i.e., $\bar{\phi}_+ \approx 10^{-2}$), then $\mathcal{S}_-$ starts to shrink, and the unstable state corresponds to a less swollen gel. If χ is chosen to be even larger (such as Figure 11(c)), then increasing $\bar{\phi}_+$ only results in the shrinking of the instability region. We note that Figure 11(b) is generated using the default parameter values used in the paper and given in (3.13a); consequently, the spinodal region in Figure 11(b) is the same one presented in Figures 3, 4(a), and 13. Furthermore, the linear stability analysis reveals that the parameter ω, related to the interfacial energy, does not influence the boundary of the region of linear stability for the system (both in the dilute and nondilute cases). However, the larger ω is, the smaller the value of largest unstable mode k_* is, where $k_* \to \infty$ as $\omega \to 0$. The initial development of instability will be thus driven by the mode $k < k_*$ corresponding to the largest positive growth rate $\lambda(k)$. Therefore, ω does not determine (in the limit where ω is

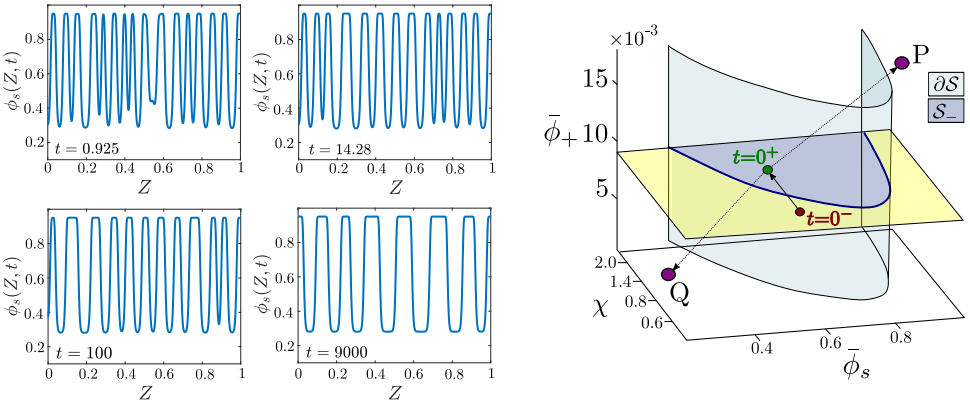

FIG. 12. *Spinodal decomposition in an isolated gel. Initially (see red point in the phase plane), the gel is equilibrated with a bath ($\phi_{0-} = 5 \times 10^{-3}$). At time $t = 0$, we isolate the gel, increase χ from 0.78 to 1.2 (see green point in the phase plane), and introduce some noise. On the left, we illustrate the evolution of the ϕ_s approximated solving numerically (3.9)–(3.10) with boundary conditions (3.12); on the right, we identify the manifold $\partial\mathcal{S}$ that divides the stable (yellow) and unstable (blue) region. The points P and Q represent the peak and the trough of the spikes. We use the values $\mathcal{G} = 0.001$, $\omega = 0.01$, $\alpha_f = 0.04$, and $\mathcal{D} = 5$.*

small compared to the size of the gel) whether spinodal decomposition occurs or not, but it can impact the spatial patterns that emerge as a result of instability.

Based on stability analysis, we now want to identify how we can drive spinodal decomposition in a gel. A standard approach is to increase the value of χ (i.e., the temperature) [15]. This exploits the fact that size of the domain $\mathcal{S}_-$ increases with χ and that moving along a vertical line in Figure 10 can push the system into the unstable regime.

We explore this scenario numerically by considering an initially homogeneous gel in equilibrium with an ionic bath (parameter values $\phi_0 = 5 \times 10^{-3}$ and $\chi = 0.78$). At time $t = 0$, the gel is isolated, and the temperature is raised so that χ increases to $\chi = 1.2$. As shown in the phase plane in Figure 12, this is sufficient to move the system from the stable region (see the red point in the phase plane of Figure 12) into the unstable regime (see the green point in the phase plane of Figure 12). As we introduced some noise in the system, growing perturbations rapidly fill the entire length of the gel and then begin to coarsen or collide, resulting in fewer and broader spikes. As shown in the phase plane in Figure 12, the peak (point P) and trough (point Q) of the spikes are located in the region of linear stability. Hence, no further instabilities develop. Over time, the evolution slows down until the pattern is almost stationary. However, we expect that, in principle, coarsening continues until only two regions remain, one in the collapsed state with $\phi_s \approx 0.3$ and the other in the swollen state with $\phi_s \approx 0.9$. These two end-state values are stable, as indicated in the rightmost panel in the figure.

6.2. Spinodal decomposition of a collapsing gel. The stability analysis, however, hints at another possible mechanism to drive spinodal decomposition in polyelectrolyte gels: increasing the concentration of co-ions in the system. Experimentally, this can be achieved by maintaining the gel in contact with the bath and increasing ϕ_0. As discussed in section 5, the ions rapidly diffuse in the gel bulk while the solvent concentration remains constant in this fast transient. Exploiting the

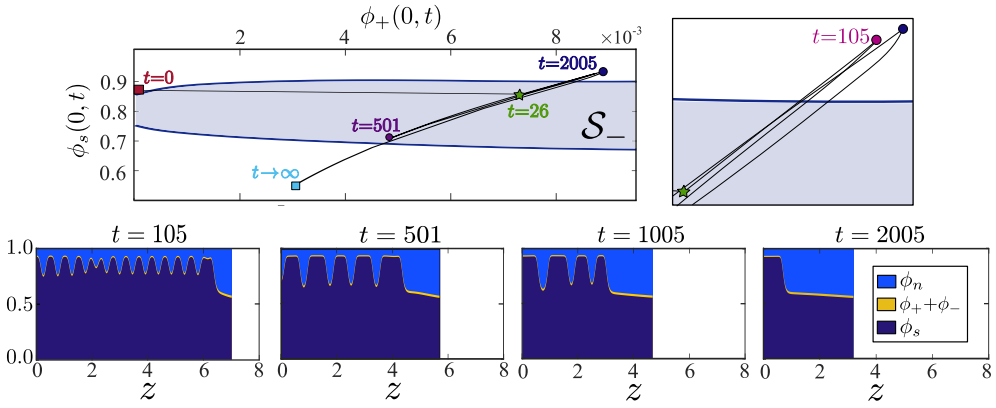

FIG. 13. *Spinodal decomposition in a collapsing gel: (top) time evolution of the gel composition* (ϕ_s, ϕ_+) *at location* $z = 0$. *The instability region* $\mathcal{S}_-$ *as predicted by the stability analysis is highlighted in blue (details on how this is computed are given in section* 6.1.2*); the panel on the right is a zoom near the green star and the blue dot to better visualize the complexity of the trajectories; (bottom) snapshot of the gel composition at different time points approximated solving numerically* (3.9)–(3.11) *with parameter values corresponding to set* 2 *in* (3.13).

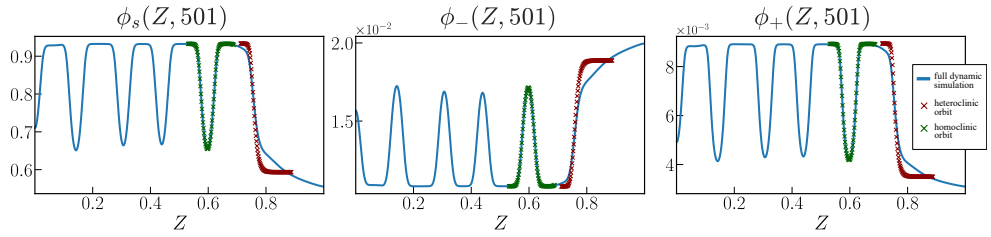

FIG. 14. *Comparison of the phase-plane solution and the numerical values of* ϕ_s, ϕ_-, *and* ϕ_+ *at time* $t = 501$ *estimated from the full dynamical simulation (same parameter values as Figure* 13*). We compare the front from the solution of the simulation of the full system (blue curve) with the approximated heteroclinic orbit for* (5.3). *The downward spikes are instead compared with the approximated homoclinic orbit (green crosses) for* (5.3). *Details on the computations can be found in section* 5.1.2.

different timescales in the system, we can therefore move along horizontal lines in the phase plane of Figure 11. For $\chi = 0.78$ (as in the simulation in section 5), changes in the instability region $\mathcal{S}_-$ occur only when $\phi_+ \sim O(10^{-3})$. Using (5.2), we obtain that ϕ_{0^+} must be increased to $\phi_{0^+} \sim O(10^{-2})$ in order to exploit the growth of $\mathcal{S}_-$.

An example of this scenario is shown in Figure 13, where we present the results of the numerical simulation for set 2 in (3.13). As expected, the ions rapidly diffuse in the gel, driving the bulk of the gel into the unstable region of the phase diagram; see $t = 26$ in the right panel of Figure 13. This results in the onset of spinodal decomposition, which gives rise to a series of solvent-depleted phases, which coarsen and collide first rapidly and then very slowly. Interestingly, at the center of each region with a low solvent concentration, there is also a high counter-ion (ϕ_-) concentration as a consequence of maintaining electroneutrality (see Figure 14). As shown in Figure 13, on a longer timescale, the depletion front propagates into the gel, consuming the array of solvent-depleted domains. When comparing with the result in Figure 5, we note that the front propagates faster in this case, with spinodal decomposition facilitating the removal of solvent from the gel.

Again, we can use phase-plane analysis (see section 5.1) for (5.3)–(5.4) to predict the structure of the collapsing gel. In doing so, we set $\tilde{\mu} = 0$ since, numerically, we find that $|\tilde{\mu}| < 10^{-3} \ll \ln \alpha_f \epsilon$. When considering the depletion front, the full model and the phase-space analysis prediction deviate slightly. As shown in Figure 14, the front obtained via phase-plane analysis is too steep, and its lower limit does not capture the actual right state of the front very well. The interface of the solvent-depleted subdomains forming in the bulk of the gel yields a better comparison with a homolinic orbit. The value of μ_s was chosen so that the minimum value for ϕ_s matches the local minimum for the PDE simulations next to the depletion front (see first panel in the figure). The homoclinic orbit matches the PDE simulations almost perfectly for all three variables displayed in the panels. A possible explanation of the higher discrepancy is that the front evolves more rapidly so that the quasi-stationary assumption underlying the phase-plane analysis breaks down. This is located near the free interface, where we have larger variations in the chemical potentials and therefore fluxes so that the quasi-stationary assumption underlying phase-plane analysis may not hold.

7. Conclusions. In this study, we have focussed on the transient dynamics of a polyelectrolyte gel in contact with a ionic bath containing a monovalent salt. Starting from a homogeneous equilibrium, we initiate the collapse of the gel by changing the surrounding salt concentration. Depending on the properties of the system, temporary patterns form with highly swollen and collapsed regions coexisting in the gel. Using the phase-field model developed in the companion paper [4], we can track the evolution of these internal interfaces, delineating the regions where the gel network has collapsed after they have formed via phase separation. We here consider the case of a one-dimensional constrained geometry, with a single free interface in contact with the bath. The model is further simplified by passing to the electroneutral limit, justified by the infinitesimal size of the electric double layer compared to the other spatial scales in the model.

Depending on the value of various model parameters, such as the Flory interaction parameter χ, the gel shear modulus $\mathcal{G}$, and the ratio of the salt concentration in the bath and the fixed charges on the polymer network $\epsilon = \phi_0/\alpha_f$, the stability properties of the homogeneous states vary. Our numerical results for the case where the gel is isolated from the bath (by using no-flux boundary conditions at the free interface) show that as the unstable homogeneous state undergoes spinodal decomposition, it forms arrays of locally collapsed solvent-depleted domains with a high concentrations of counter-ions. These eventually coarsen into a new stable equilibrium.

When in contact with the bath, the gel is sensitive to the salt concentration ϕ_0 in the surrounding fluid. Increasing ϕ_0 initiates and drives the collapse of the gel. This process is characterized by a depletion front that forms via phase separation and travels into the gel. Using phase-plane analysis, we are able to show that the depletion front selects the homogeneous states at its front and rear. These are always linearly stable. In the spinodally unstable regime, the emerging structure of collapsed solvent-depleted domains are well approximated by homoclinic solutions of the DAE system and are consumed by the depletion front that propagates through the gel on a faster timescale than the coarsening process.

Even though our analysis is currently only one-dimensional, it sheds light on the possibility of observing these patterns experimentally. Depending on parameter settings, the transient patterns with a high concentration of ϕ_- in the collapsed and a high concentration of ϕ_+ in the swollen regions are in principle observable. Our

approach provides a template for how mathematical techniques such as phase-plane analysis and stability analysis can elucidate the notoriously complicated models for polyelectrolytes beyond numerical simulations, particularly when employed in combination.

An important consequence of our approach is that fundamental quantities, such as the velocity of the localized front, can now be predicted using an asymptotic analysis based on our approximation of the depletion front. Our analysis can also be easily generalized to settings that account, for example, for multivalent salts and concentration-dependent permittivity and may allow to capture further scenarios of collapse. This will be carried out in our forthcoming work in the one-dimensional setting as well as in higher-dimensional formulations.

REFERENCES

[1] T. Budtova and P. Navard, *Swelling kinetics of a polyelectrolyte gel in water and salt solutions: Coexistence of swollen and collapsed phases*, Macromolecules, 31 (1998), pp. 8845–8850, https://doi.org/10.1021/ma981174s.

[2] D. Buenger, F. Topuz, and J. Groll, *Hydrogels in sensing applications*, Prog. Polym. Sci., 37 (2012), pp. 1678–1719, https://doi.org/10.1016/j.progpolymsci.2012.09.001.

[3] S. Cai and Z. Suo, *Mechanics and chemical thermodynamics of phase transition in temperature-sensitive hydrogels*, J. Mech. Phys. Solids, 59 (2011), pp. 2259–2278.

[4] G. L. Celora, M. G. Hennessy, A. Münch, B. Wagner, and S. L. Waters, *A kinetic model of a polyelectrolyte gel undergoing phase separation*, J. Mech. Phys. Solids, 160 (2022), 104771.

[5] S. Chaterji, I. K. Kwon, and K. Park, *Smart polymeric gels: Redefining the limits of biomedical devices*, Prog. Polym. Sci., 32 (2007), pp. 1083–1122, https://doi.org/10.1016/j.progpolymsci.2007.05.018.

[6] H. Chen, M.-C. Calderer, and Y. Mori, *Analysis and simulation of a model of polyelectrolyte gel in one spatial dimension*, Nonlinearity, 27 (2014), pp. 1241–1285, https://doi.org/10.1088/0951-7715/27/6/1241.

[7] M. S. Dimitriyev, Y.-W. Chang, P. M. Goldbart, and A. Fernández-Nieves, *Swelling thermodynamics and phase transitions of polymer gels*, Nano Futures, 3 (2019), 042001, https://doi.org/10.1088/2399-1984/ab45d5.

[8] A. Dobrynin, *Theory and simulations of charged polymers: From solution properties to polymeric nanomaterials*, Curr. Opin. Colloid Interface Sci., 13 (2008), pp. 376–388, https://doi.org/10.1016/j.cocis.2008.03.006.

[9] M. Doi, *Gel dynamics*, J. Phys. Soc. Jpn., 78 (2009), 052001.

[10] F. G. Donnan, *The theory of membrane equilibria*, Chem. Rev., 1 (1924), pp. 73–90, https://doi.org/10.1021/cr60001a003.

[11] A. D. Drozdov, A. A. Papadimitriou, J. H. Liely, and C. G. Sanporean, *Constitutive equations for the kinetics of swelling of hydrogels*, Mech. Mater., 102 (2016), pp. 61–73, https://doi.org/10.1016/j.mechmat.2016.08.012.

[12] K. Dusek and D. Patterson, *Transition in swollen polymer networks induced by intramolecular condensation*, J. Polym. Sci. A-2 Polym. Phys., 6 (1968), pp. 1209–1216, https://doi.org/10.1002/pol.1968.160060701, https://onlinelibrary.wiley.com/doi/pdf/10.1002/pol.1968.160060701.

[13] A. Estévez-Torres and D. Baigl, *DNA compaction: Fundamentals and applications*, Soft. Matter, 7 (2011), 6746. https://doi.org/10.1039/c1sm05373f.

[14] M. G. Hennessy, G. L. Celora, A. Münch, B. Wagner, and S. L. Waters, *The Electric Double Layer at the Interface between a Polyelectrolyte Gel and Salt Bath*, preprint, arXiv:2201.11554, 2022.

[15] M. G. Hennessy, A. Münch, and B. Wagner, *Phase separation in swelling and deswelling hydrogels with a free boundary*, Phys. Rev. E, 101 (2020), 032501, https://doi.org/10.1103/PhysRevE.101.032501, https://link.aps.org/doi/10.1103/PhysRevE.101.032501.

[16] W. Hong, *Continuum Models of Stimuli-Responsive Gels*, Springer-Verlag, Berlin, 2012, pp. 165–196.

[17] W. Hong, X. Zhao, and Z. Suo, *Large deformation and electrochemistry of polyelectrolyte gels*, J. Mech. Phys. Solids, 58 (2010), pp. 558–577.

[18] F. Horkay, I. Tasaki, and P. J. Basser, *Effect of monovalent-divalent cation exchange on the swelling of polyacrylate hydrogels in physiological salt solutions*, Biomacromolecules, 2 (2001), pp. 195–199, https://doi.org/10.1021/bm0056153.

[19] J. Hua, M. K. Mitra, and M. Muthukumar, *Theory of volume transition in polyelectrolyte gels with charge regularization*, J. Chem. Phys., 136 (2012), 134901. https://doi.org/10.1063/1.3698168.

[20] J. M. Huyghe and J. D. Janssen, *Quadriphasic mechanics of swelling incompressible porous media*, Int. J. Eng. Sci., 35 (1997), pp. 793–802, https://doi.org/10.1016/S0020-7225(96)00119-X.

[21] A. R. Khokhlov and E. Y. Kramarenko, *Weakly charged polyelectrolytes: Collapse induced by extra ionization*, Macromolecules, 29 (1996), pp. 681–685, https://doi.org/10.1021/ma946426d.

[22] E. Kokufuta, *Polyelectrolyte gel transitions: Experimental aspects of charge inhomogeneity in the swelling and segmental attractions in the shrinking*, Langmuir, 21 (2005), pp. 10004–10015, https://doi.org/10.1021/la050530e.

[23] H. J. Kwon, Y. Osada, and J. P. Gong, *Polyelectrolyte gels-fundamentals and applications*, Polym. J., 38 (2006), pp. 1211–1219, https://doi.org/10.1295/polymj.PJ2006125.

[24] O. Lewis, J. Keener, and A. Fogelson, *Electrodiffusion-mediated swelling of a two-phase gel model of gastric mucus*, Gels, 4 (2018), 76, https://doi.org/10.3390/gels4030076.

[25] M. P. Lutolf and J. A. Hubbell, *Synthetic biomaterials as instructive extracellular microenvironments for morphogenesis in tissue engineering*, Nat. Biotechnol., 23 (2005), pp. 47–55, https://doi.org/10.1038/nbt1055.

[26] E. S. Matsuo and T. Tanaka, *Patterns in shrinking gels*, Nature, 358 (1992), pp. 482–485, https://doi.org/10.1038/358482a0.

[27] J. L. Mccoy and M. Muthukumar, *Dynamic light scattering studies of ionic and nonionic polymer gels with continuous and discontinuous volume transitions*, J. Polym. Sci. B Polym. Phys., 48 (2010), pp. 2193–2206, https://doi.org/10.1002/polb.22101.

[28] Y. Mori, H. Chen, C. Micek, and M.-C. Calderer, *A dynamic model of polyelectrolyte gels*, SIAM J. Appl. Math., 73 (2013), pp. 104–133.

[29] M. Mussel and F. Horkay, *Experimental evidence for universal behavior of ion-induced volume phase transition in sodium polyacrylate gels*, J. Phys. Chem. Lett., 10 (2019), pp. 7831–7835, https://doi.org/10.1021/acs.jpclett.9b03126.

[30] C. Ning, Z. Zhou, G. Tan, Y. Zhu, and C. Mao, *Electroactive polymers for tissue regeneration: Developments and perspectives*, Prog. Polym. Sci., 81 (2018), pp. 144–162, https://doi.org/10.1016/j.progpolymsci.2018.01.001.

[31] S. Puri and K. Binder, *Surface-directed phase separation with off-critical composition: Analytical and numerical results*, Phys. Rev. E, 66 (2002), 061602, https://doi.org/10.1103/PhysRevE.66.061602.

[32] D. Roshal, O. Konevtsova, A. Losdorfer Bozic, R. Podgornik, and S. Rochal, *pH-induced morphological changes of proteinaceous viral shells*, Sci. Rep., 9 (2019), 5341, https://doi.org/10.1038/s41598-019-41799-6.

[33] E. Sato Matsuo and T. Tanaka, *Kinetics of discontinuous volume-phase transition of gels*, J. Chem. Phys., 89 (1988), pp. 1695–1703.

[34] T. K. Sherwood, R. L. Pigford, and C. R. Wilke, *Mass Transfer*, McGraw-Hill, New York, 1975.

[35] C. E. Sing, J. W. Zwanikken, and M. Olvera de la Cruz, *Effect of ion-ion correlations on polyelectrolyte gel collapse and reentrant swelling*, Macromolecules, 46 (2013), pp. 5053–5065, https://doi.org/10.1021/ma400372p.

[36] S. Sircar, J. P. Keener, and A. L. Fogelson, *The effect of divalent vs. monovalent ions on the swelling of Mucin-like polyelectrolyte gels: Governing equations and equilibrium analysis*, J. Chem. Phys., 138 (2013), 014901. https://doi.org/10.1063/1.4772405.

[37] M. A. Stuart, W. T. Huck, J. Genzer, M. Müller, C. Ober, M. Stamm, G. B. Sukhorukov, I. Szleifer, V. V. Tsukruk, M. Urban, F. Winnik, S. Zauscher, I. Luzinov, and S. Minko, *Emerging applications of stimuli-responsive polymer materials*, Nat. Mater., 9 (2010), pp. 101–113, https://doi.org/10.1038/nmat2614.

[38] T. Tanaka, *Collapse of gels and the critical endpoint*, Phys. Rev. Lett., 40 (1978), pp. 820–823, https://doi.org/10.1103/PhysRevLett.40.820, https://link.aps.org/doi/10.1103/PhysRevLett.40.820.

[39] T. Tomari and M. Doi, *Hysteresis and incubation in the dynamics of volume transition of spherical gels*, Macromolecules, 28 (1995), pp. 8334–8343.

[40] Y. Yu, C. M. Landis, and R. Huang, *Salt-induced swelling and volume phase transition of polyelectrolyte gels*, J. Appl. Mech., 84 (2017), 051005, https://doi.org/10.1115/1.4036113.

[41] R. Zandi, B. Dragnea, A. Travesset, and R. Podgornik, *On virus growth and form*, Phys. Rep., 847 (2020), pp. 1–102, https://doi.org/10.1016/j.physrep.2019.12.005.

[42] A. Y. Zubarev, F. A. Blyakhman, G. H. Pollack, P. Gusev, and A. P. Safronov, *Self-similar wave of swelling/collapse phase transition along polyelectrolyte gel*, Macromol. Theory Simul., 13 (2004), pp. 697–701, https://doi.org/10.1002/mats.200400027.